Journal of Applied Physics

Determination of thermophysical properties and density volume fractions of Al_2O_3/Y-ZrO_2 layered composite materials using transient thermography and two-stage inverse nonlinear heat conduction analysis

Cite as: J. Appl. Phys. **127**, 045110 (2020); https://doi.org/10.1063/1.5116709
Submitted: 28 June 2019 . Accepted: 26 December 2019 . Published Online: 31 January 2020

Sahar Kooshki, Andreas Mandelis, Mahmoud Khodadad, Amir Khosravifard, and Alexander Melnikov

AIP Publishing

Journal of Applied Physics ARTICLE scitation.org/journal/jap

Determination of thermophysical properties and density volume fractions of Al_2O_3/Y-ZrO_2 layered composite materials using transient thermography and two-stage inverse nonlinear heat conduction analysis

Cite as: J. Appl. Phys. **127**, 045110 (2020); doi: 10.1063/1.5116709
Submitted: 28 June 2019 · Accepted: 26 December 2019 ·
Published Online: 31 January 2020

Sahar Kooshki,[1,2] Andreas Mandelis,[2] Mahmoud Khodadad,[1,a)] Amir Khosravifard,[3] and Alexander Melnikov[2]

AFFILIATIONS

[1]Department of Mechanical Engineering, Yazd University, Yazd 8915818411, Iran
[2]Center for Advanced Diffusion-Wave and Photoacoustic Technologies (CADIPT), Department of Mechanical and Industrial Engineering, University of Toronto, 5 King's College Road, Toronto, Ontario M5S 3G8, Canada
[3]Department of Mechanical Engineering, Shiraz University, Shiraz 71936, Iran

[a)]khodadad@yazd.ac.ir

ABSTRACT

In the present study, transient thermography, a nondestructive imaging technique, is applied to evaluate the transient temperature response in a graded medium without the use of embedded thermocouples. A layered composite sample was fabricated from Al_2O_3 and Y-ZrO_2 powders using powder metallurgy (PM). This sample was irradiated on one side with a direct current laser while the transient temperature was measured along its depth by a midinfrared camera. Also, a MATLAB code based on the truly meshless radial point interpolation method (t-RPIM) was developed and implemented to solve the problem of quasilinear transient heat transfer in PM solids. In the t-RPIM formulation, the Cartesian transformation method and the Crank-Nicolson scheme were used for the evaluation of domain integrals and time discretization, respectively, thereby yielding a truly mesh-free technique. In the conducted experiment, the thermophysical properties were assumed to be independent of temperature because of the small amount of temperature increase. These properties and the volume fractions of the constituent powders were determined using a combination of the t-RPIM and the damped Gauss-Newton method in an inverse analysis. Good agreement was found between the measured temperature and the reconstructed temperature profile using the identified thermal parameters and volume fractions, thus validating the accuracy and ability of the applied t-RPIM as a tool in an inverse scheme to solve the inverse transient heat conduction problem in nonhomogeneous media.

I. INTRODUCTION

Nowadays, scientists and engineers recognize the importance of the use of innovative materials for economic and environmental reasons.[1] Functionally graded materials (FGMs) are new generations of composite materials, which can help achieve desirable structural behavior. This makes graded materials suitable candidates for numerous applications in aerospace, bioengineering, etc.[2] The gradual changes in the volume fraction of the constituents of an FGM provide continuously graded macroscopic properties, such as hardness, wear resistance, corrosion resistivity, thermal conductivity, specific heat, etc., that are critical for thermal barrier coatings (TBCs), thermal protection of space capsule re-entry, furnace liners, body armor, piezoelectric actuators, and electromagnetic sensors.[3–6] Other applications include high current connectors and capacitors.[7,8] In addition, functionally graded electrodes for solid oxide fuel cells (SOFCs) are widely used in the energy sector.[9]

In this article, the thermal behavior of a layered composite sample as a representative of graded materials is studied.

Considering the increasing applications of graded materials, the development of reliable methods for the evaluation of their thermal response is critical. Usually, in a graded material, there is a gradual or stepwise change of properties perpendicular to the body surface, so many traditional steady-state evaluation techniques like those for thermal conductivity measurement cannot be used.[10] Standard nondestructive evaluation (NDE) techniques such as photothermal radiometery (PTR), acoustic emission (AE), and eddy current have been used in the evaluation of graded materials. Measurements of their thermal diffusivity and thermal effusivity have been made using PTR.[10–12] In the PTR technique, the front surface of the sample is heated using a modulated heat source. The thermal-wave response is measured from the front surface as a function of frequency, and the thermal-wave amplitude and phase can be used for the reconstruction of thermal diffusivity depth profiles. In addition, thermal shock tests with *in situ* acoustic emission are used to study the cracking behavior of plasma sprayed functionally graded thermal barrier coatings.[13] Nondestructive techniques such as infrared imaging and ultrasonic testing are also used for defect detection in FGMs.[14]

To evaluate the performance of graded materials, it is crucial to develop tools to reconstruct their thermal properties. Since the first step in the reconstruction process is having a reliable numerical method that could calculate the temperature distribution, validation of the t-RPIM[15,16] (Appendix A) through an experimental study is valuable. Generally speaking, much work has been done on the reconstruction of thermal properties in graded materials using inverse algorithms in combination with numerical methods.[17–19] Furthermore, having a reliable numerical method to predict the thermal response of the graded materials provides the possibility of identification of the shape and location of voids and inclusions in the graded materials using inverse algorithms in diagnostic and structural health monitoring (SHM) applications. For example, the boundary element method (BEM) was applied in combination with the Particle Swarm Optimization (PSO) algorithm[20] to estimate the thermal conductivity and shape of an inclusion inside a solid body under steady-state conditions.

Photothermal imaging is a noncontact, fast, and reliable diagnostic method.[21] It is also used in biomedical applications such as detection of early dental caries with better sensitivity than radiography.[22,23] In this work, infrared thermographic imaging was used to measure the transient temperature distribution in a layered medium irradiated by a laser beam without using embedded thermocouples. The experimental results were interpreted in terms of a theoretical analysis of the nonlinear transient temperature response in a quasi-linear limit of temperature rise and its numerical implementation. Best fits of the theory to the data using an inverse algorithm allow the estimation of material properties like thermal conductivity and specific heat and their distribution along the specimen depth coordinate. In order to generalize this method to continuously graded materials, a nonlinear volume fraction function like an exponential with a limited number of parameters for effective property calculations in the FGM and evaluation of these parameters in an inverse algorithm has been used in the literature[18,24–26] and could be applied here, too. However, in this article, only a layered composite sample is studied. In general, the properties of materials manufactured/fabricated using the powder metallurgy (PM) method depend on the processing parameters; therefore, they require determination by a case-by-case analysis.[10] Toward this goal, an approximation of the temperature dependence of the constituent materials thermophysical properties was assumed based on literature values. These empirical relations for the variation of the thermophysical properties with temperature showed that their change with temperature within the range of our experiments was negligible. As a result, constant values were adopted for the thermophysical properties of the constituent materials. Since the parameters of the PM process can have a significant effect on the thermophysical properties of the fabricated sample, identification of the actual properties of the fabricated samples using the PM techniques is quite important. Therefore, based on the thermographically measured temperature depth profile of the fabricated sample, its thermophysical properties were determined through an inverse analysis in this work. The theory further allowed the estimation of volume fractions of the constituent materials as a function of depth. Validation of the determined thermal property and volume fraction values was performed through a comparison of directly measured and calculated temperature depth profiles.

II. MATERIALS

A. Preparation and processing

Fabrication of an Al_2O_3/Y-ZrO_2 graded composite that has both superior alumina properties (i.e., excellent hardness and wear resistance) and zirconia characteristics (i.e., remarkable toughness and strength) has been widely pursued for medical applications.[2] There are several reports on the application of this family of graded materials for the fabrication of hip or knee prostheses due to their excellent biocompatibility.[27,28] There exist various methods of graded materials fabrication including both classical and modern techniques such as the PM method,[3–5] coating processes,[2] centrifugal casting,[29,30] thermal spraying,[31,32] plasma methods (spraying and welding), etc. The most appropriate graded materials' fabrication method can be chosen based on the material combination, the type of the transition function, and the geometry of the desired components.[31] The transition function in a graded material determines a property gradient, which is usually the volume fraction of the constituents as a function of one or more coordinates. Among the aforementioned methods, the PM method enables the fabrication of materials with good control of chemical composition and microstructure.[33] Processing parameters such as temperature, time, and pressure have a significant influence on the properties of the graded materials produced using the PM method[2] used in this work because of its simplicity and the availability of the required equipment. It involves the preparation of the mixture of powder materials according to a predesigned dispersion formulation, stacking, and finally sintering.[34] α-Aluminum oxide (α-Al_2O_3) nanopowder (99.85%, 40 nm grain size, Inframat Advanced Materials, USA) and commercial 5.3 wt. % (3 mol. %) tetragonal yttria-stabilized zirconia powder (TZ-3YB, from TOSOH, Japan) were used as the raw materials. The TOSOH powder shapes were 100% tetragonal. The theoretical density of the α-Al_2O_3 powder is 3.97 g/cm^3 and that of the TZ-3YB powder is 6.05 g/cm^3.

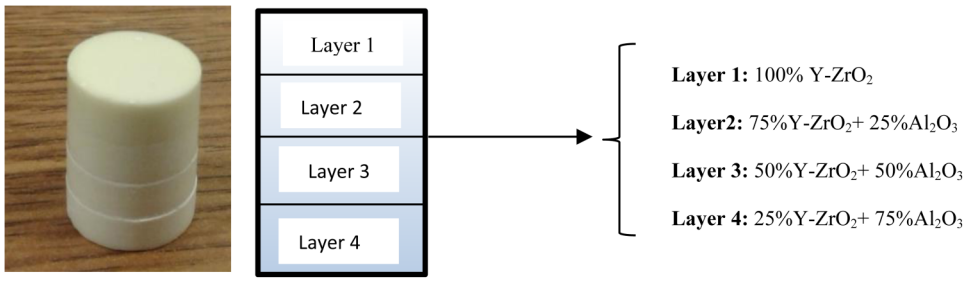

FIG. 1. Layer sequence in the layered composite sample.

A 4-layer sample with 5-mm thickness of each layer was made. Figure 1 shows a schematic of the Y-ZrO_2 and Al_2O_3 layer composition in this sample. Figure 2 shows the flow chart of the manufacturing process of the Al_2O_3/Y-ZrO_2 sample. The powders were compacted by uniaxial pressure without a binder. After putting all the layer mixtures in the die (two centimeter diameter), the powders were cold pressed at 70 MPa for three minutes into a disk-shaped specimen. Sintering of the green sample was done according to the sintering schedule from TOSOH (heating at 100 °C/h, sintering at 1500 °C for 2 h, and natural cooling in a furnace at 2 °C/min) in a Barnstead/Thermolyne model F46120CM furnace. Several samples were fabricated and then examined for the possible presence of deep cracks at the interfaces between layers. This was done through irradiation with a low frequency modulated laser beam incident normal to the surface of the upper layer and the observation of the thermal-wave distribution from the side surface using a 3–5 μm spectral band midinfrared (MIR) camera (A6700sc, FLIR, USA). In the samples that were deeply cracked in the depth direction, the thermal-wave profile decreased abruptly behind the crack due to the large thermal impedance. The best quality sample was thus selected for the studies reported in this work.

B. Thermophysical properties of Al_2O_3/Y-ZrO_2 layered composites

To measure the effective thermophysical properties at any point in the sample, the rule of mixture (ROM) homogenization technique[15,16] was employed. According to the ROM, widely used for its simplicity,[15] the effective properties at each point can be calculated from the following expression:

$$p = p_1 v_1 + p_2 v_2, \tag{1}$$

where v_1 and v_2 are the volume fractions of materials 1 and 2, respectively, and p_1 and p_2 are the corresponding values of the investigated property of each material. For transient heat conduction analysis of a graded material, one needs to know the density, thermal conductivity, and specific heat of the constituents, i.e., the pure sintered alumina and the pure sintered zirconia. As the actual density is important for porosity measurements, pure samples from each powder with 2 cm diameter and 4–6 mm thickness were fabricated with the same sintering schedule as used for the nonhomogeneous sample. The density of each type of specimen was measured using the Archimedes principle, with water as the immersion medium. The actual densities of the pure Al_2O_3 and the pure Y-ZrO_2 sample were found to be 3.8 g/cm^3 and 5.9 g/cm^3, respectively. The relation between density and porosity is given by

$$\varepsilon = \left[1 - \frac{\rho_a}{\rho_s}\right] \times 100, \tag{2}$$

which allows the calculation of the porosity percent in the samples from their measured and their theoretical densities.[35] In Eq. (2), ε is the porosity %, ρ_a is the actual density (with porosity), and ρ_s is the theoretical density (without porosity). Porosities for the pure Al_2O_3 and the pure Y-ZrO_2 sample were found to be 2.47% and 4.28%, respectively. Therefore, both samples were considered to be

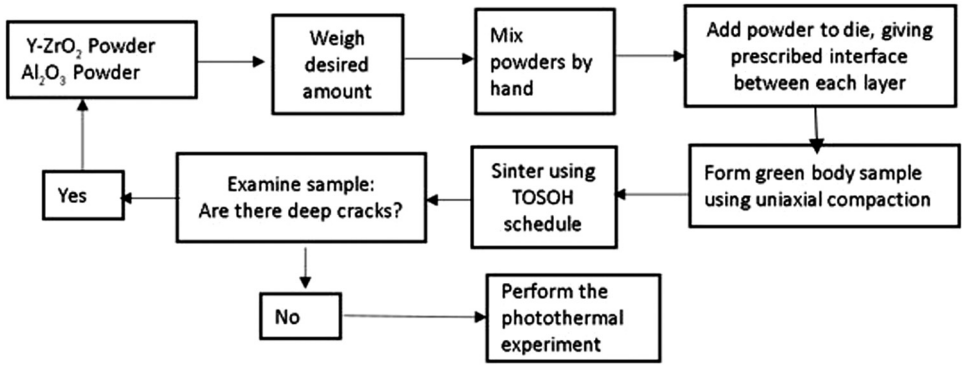

FIG. 2. Flow chart of the manufacturing process.

fully dense. The low percent of porosity in the samples was further confirmed by their optical transparency. It is known that only extremely dense samples can transmit light well due to the fact that pores are efficient light scatterers.[36]

Effective defining factors of thermal properties of sintered samples include sintering schedule, porosity, microstructure, grain size, purity, and composition.[36–40] Therefore, the actual values of these properties in sintered samples cannot be found in the literature; they must be measured or reconstructed on a case-by-case basis. For their determination, the temperature dependent thermal conductivity and specific heat of sintered alumina and sintered zirconia with similar, but not exactly the same, sintering parameters, were adopted from the literature.[38,40–42]

Temperature dependencies of the thermal conductivity and specific heat for high purity (min. 99.6% Al_2O_3) sintered alumina with porosity 3%–6% and density 3.75–3.85 g/cm^3 are given as follows:[41]

$$k(\mathrm{T})_{\mathrm{Al_2O_3}} = 5.5 + 34.5 \times \exp\{-0.0033 \times (T - 273)\} \quad (\text{in } \mathrm{W/m\,K}, \quad 298 - 1573\,\mathrm{K}), \tag{3a}$$

$$c(T)_{\mathrm{Al_2O_3}} = 1.0446 + 1.742 \times 10^{-4} \times T - 2.796 \times 10^{4} \times T^{-2} \quad (\text{in } J/\mathrm{g\,K}, \quad 298 - 1737\,\mathrm{K}). \tag{3b}$$

The thermal conductivity and specific heat of stabilized zirconia have been the subject of numerous experimental investigations.[36,39,42–46] Schlichting *et al.* measured the thermal conductivity of dense and porous yttria-stabilized zirconia (YSZ) ceramics as a function of temperature in the range of 25–1000 °C.[42] The most important factor in the thermal conductivity of YSZ is its yttria content[36,42,46] and microstructures.[39] After performing a polynomial curve fitting on the thermal conductivity measurements of fully dense (porosity less than 6%) 3 mol. % YSZ,[42] the following relation was obtained:

$$k(\mathrm{T})_{\mathrm{ZrO_2}} = 2.2767 + 0.0056 \times T - 1.2621 \times 10^{-5} \times T^2 + 9.9895 \times 10^{-9} T^3 - 2.7527 \times 10^{-12} \times T^4 \quad (\mathrm{W/m\,K}). \tag{4a}$$

The specific heat capacity of TZ-3YB was determined by Taylor *et al.* using differential scanning calorimetry[38] in an Omnitherm DSC 1500 apparatus with sapphire as the baseline standard. That study indicated that the specific heat is insensitive to the microstructure. Polynomial fitting on the specific heat data[38] was performed, and the following relation was obtained:

$$c(T)_{\mathrm{ZrO_2}} = 239.3402 + 1.052\,69 \times T - 0.001\,12 \times T^2 + 5.622\,17 \times 10^{-7} \times T^3 - 1.07881 \times 10^{-10} \times T^4 \quad (\mathrm{J\,kg^{-1}\,K^{-1}}). \tag{4b}$$

The calculation of the thermal conductivity and specific heat of alumina and zirconia from Eqs. (3a) to (4b) at room temperature (25 °C) and at the maximum temperature during the experiment according to Fig. 5 (32 °C) showed that the total thermophysical parameter change with temperature during the experiment was less than 1%. Consequently, the aforementioned thermal property constant value hypothesis of the constituent materials was validated through the direct measurement and subsequently used in the development of the theoretical inverse heat conduction problem and the associated computational analysis of the experimental results.

III. EXPERIMENTAL AND RESULTS

A Cr layer (300 nm thick) was deposited on the surface of the sample using an AJA International ATC Orion 5 Sputter Deposition System to turn the transparent specimen surface opaque. The specimen was polished to a 1-μm final finish using routine ceramographic methods before sputtering. For measuring the transient temperature in the sample, a CW 808 nm laser diode (JOLD-30-CPXF-1L) beam was shone normal to the circular cross section of the sample surface (Fig. 3). A uniform laser beam distribution was employed for heating the front surface of the sample. This was achieved by using a diffuser in front of the beam which homogenized the exiting power. The collimated laser beam was spread and homogenized by a microlens array with intensity variations <5% across that area. Therefore, constant laser intensity impinged on the front surface, and a constant heat flux was assumed in the numerical modeling. The MIR camera operating at 104 fps was used to capture the photothermal transient depth profile. The MIR camera FLIR A6753sc was calibrated by FLIR Systems, Inc., for measurements of relative temperature. A thermocouple was attached to the back end of the sample to measure the initial temperature of the specimen at the beginning of all

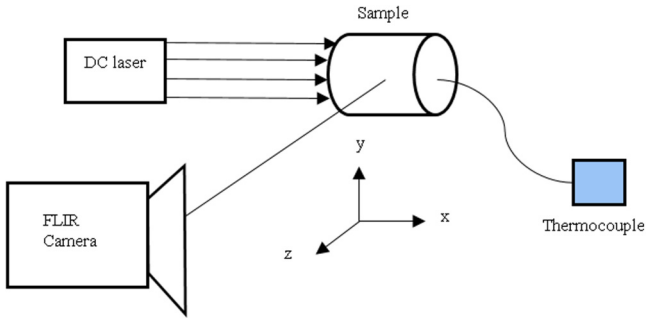

FIG. 3. The thermographic setup. The collimated CW laser operated in the DC (unmodulated) mode.

measurements. Comparison of the measured temperature with a thermocouple at the onset of measurements led to a MIR image that shows a constant temperature along four layers with a deviation of about 0.2 °C. Therefore, it was concluded that the emissivities of four layers were very close and increasing the sample temperature by a few degrees during the laser irradiation experiment was not expected to create considerable differences among the emissivities of the four layers. The thermographic image pixel dependencies were analyzed theoretically in order to extract the temperature at each depth. Then, the measured temperature data in combination with the calculated temperatures were used to determine the thermophysical properties such as thermal conductivity and specific heat of the fabricated sample in the temperature range of the experiment in an inverse problem analysis owing to the coordinate dependence of the thermophysical properties and the density. A two-stage inverse problem theory was developed which further allowed the determination of volume fractions of the constituent materials in the sample. The depth dependencies of the thermophysical properties and the density were estimated using the ROM homogenization technique. Although the proposed method in this paper is used to identify the properties of layered samples, for identification of the thermal properties in an FGM, one could assume a nonlinear transition function for the FGM properties like an exponential or power function and identify the parameters of that function using an inverse analysis.

A layered sample with graded properties only in the depth direction was tested under transient heating conditions, with the direct current (DC) laser irradiating one surface of the specimen while the other surfaces were exposed to the ambient with free convection. The photothermal problem was modeled in 2D due to the axial symmetry. Considering both convection and radiation effects, the total heat convection coefficient is the summation of the convection heat transfer coefficient (h_c) and the effective convection heat transfer coefficient for radiation (h_r), which is calculated from Eq. (5),[47]

$$h_r = \sigma\varepsilon_r[(T + T_\infty)(T^2 + T_\infty^2)]. \quad (5)$$

In Eq. (5), $\sigma = 5.6703 \times 10^{-8}\,\mathrm{W/m^2\,K^4}$ is the Stefan-Boltzmann constant and ε_r is the surface emissivity. Also, T_∞ is the ambient temperature, which was 25 °C. The total convection heat transfer coefficient is the summation of both convection and radiation effects: $h = h_c + h_r$. The convection heat transfer coefficient for the sample was calculated using the average diameter of the sample (diameter = 16.5 mm); the initial surface temperature, which was 26.6 °C; and the ambient temperature. The change in the latter was small on the order of 6 °C; therefore, a constant h_c value was assumed and estimated to be $h_c = 7.6\,\mathrm{W/m^2\,K}$ using the equation of $h_c = Nuk/D$, where Nu is the Nusselt number for a horizontal cylinder in the laminar free convection conditions calculated according to the Churchill and Chu formula,[48] k is the thermal conductivity for air, and D is the sample diameter. For calculation of the effective convection heat transfer coefficient for radiation (with the assumption of high emissivity surfaces), $h_r = 6\,\mathrm{W/m^2\,K}$ is obtained. Therefore, the total convection heat transfer coefficient is $h = 13.6\,\mathrm{W/m^2\,K}$, which is used in the calculations.

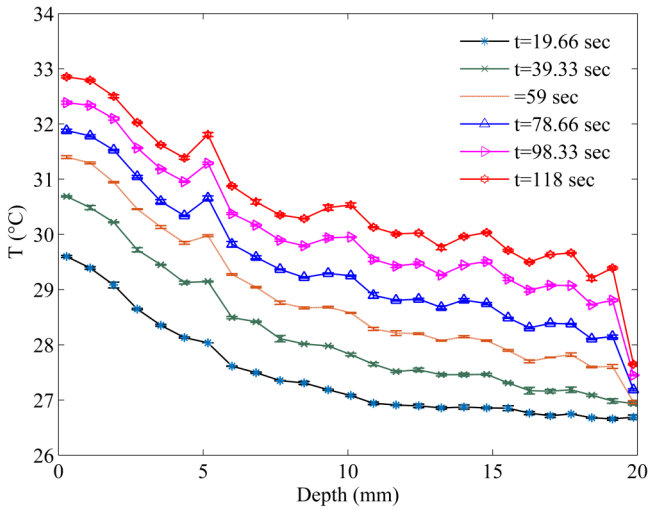

FIG. 4. Experimental temperature distribution in the sample along the depth at y = 11.3 mm.

The experimental temperature depth profiles were measured using the MIR camera with no embedded thermocouples and they are plotted in Fig. 4 at various time instants. The trends of experimental transient temperature depth distributions at each recorded instant are similar, with temperatures increasing at longer times. These depth profile similarities show that the effect of temperature change on thermophysical properties during the heating process was not considerable.

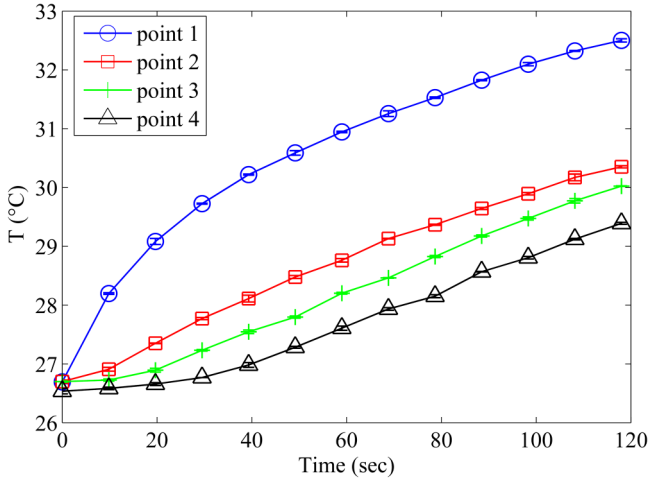

FIG. 5. Experimental temperature history for representative points in various layers of the sample: (point 1) In the 1st layer at x = 1.9 mm, y = 11.3 mm; (point 2) in the 2nd layer at x = 7.6 mm, y = 11.1 mm; (point 3) in the 3rd layer at x = 12.5 mm, y = 10.7 mm; (point 4) in the 4th layer at x = 19.1 mm, y = 10.9 mm.

To examine the effect of powder layer composition on temperature evolution, four points in four different layers were considered (Fig. 5). Figure 5 shows that the rate of temperature change in the first layer, which is pure Y-ZrO_2, is maximum while the rate decreases with the increase of Al_2O_3 content in the deeper layers. Also, the temperature of different layers of the sample changed between 2 and 6 °C. Therefore, from this perspective, too, it is reasonable to expect that the thermal properties of the sample did not change with temperature, consistently with the results in Fig. 4. On the other hand, according to Fig. 4, at each instant, there was approximately 3 °C temperature decrease from the first to the fourth layer which was ~50% of the total temperature change during the experiment. Therefore, at each moment, there was a significant, measurable temperature change in the sample and measurable temperature sensitivity with respect to depth. As a consequence, the determination of the spatial dependence of thermophysical properties in the sample was studied in an inverse analysis presented in Sec. V. Determination of the depth dependence of thermophysical properties can yield a better understanding of layer parameters and their depth profiles as feedback to graded sample fabrication/manufacturing and it shows how the thermal behavior of this nonhomogeneous sample changes with depth.

IV. THEORY OF LASER-INDUCED TEMPERATURE DISTRIBUTION IN NONHOMOGENEOUS SOLIDS

A. The photothermally induced transient nonlinear heat conduction boundary value problem

The governing equation of transient heat conduction in a thermophysically nonhomogeneous solid can be written as

$$\nabla \cdot (k(\boldsymbol{x}, \boldsymbol{T})\nabla T(\boldsymbol{x}, T)) = \rho(\boldsymbol{x}, \boldsymbol{T})c(\boldsymbol{x}, \boldsymbol{T})\partial T(\boldsymbol{x}, T)/\partial t, \qquad (6)$$

where T is the temperature, ρ is the mass density, c is the specific heat, and k is the thermal conductivity of the solid. The nonlinearity in the present problem arises from the coordinate dependence of the density and the thermophysical parameters k and c. The boundary conditions are shown in Fig. 6. The Γ_1 boundary was heated photothermally with the DC laser generating constant heat flux. All other boundaries were exposed to air with convection boundary conditions

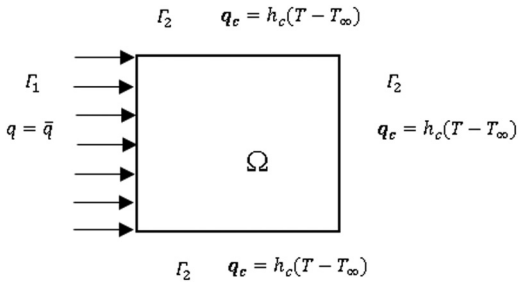

FIG. 6. Domain and boundary conditions of nonhomogeneous solids.

and initial and boundary conditions as follows:

$$\begin{aligned} &T(\boldsymbol{x}, 0) = T_0(\boldsymbol{x}) && \text{in the domain } \Omega, \\ &-k(\nabla T(\boldsymbol{x}, t) \cdot \boldsymbol{n}) = \bar{q} && \text{on the boundary with constant heat flux } \boldsymbol{x} \in \Gamma_1, \\ &q_c = h(T - T_\infty) && \text{on the boundaries with convection boundary condition } \boldsymbol{x} \in \Gamma_2, \end{aligned}$$

where $\boldsymbol{n}$ is the unit outward vector to the boundary, T_0 is the initial temperature, T_∞ is the ambient temperature distribution, h is the total convection heat transfer coefficient, and $\bar{q}$ is the applied heat flux to the boundary Γ_1.

In general, the material properties of graded media are space and mostly temperature dependent. Consequently, the solution of the transient heat transfer problem in such media is complicated, especially when the geometry of the domain is somewhat complex. Several numerical methods have been used for the study of nonlinear transient heat transfer in graded materials such as the finite element method (FEM), the BEM, and also meshless methods (MMs). Because of the highly mesh-dependent characteristics, the FEM has many inherent shortcomings, especially in the re-meshing processes when the elements become highly distorted. This may be a serious disadvantage in handling problems with large gradients, crack propagations, large deformations, etc.[15] The BEM method only requires information from the nodes on the boundary instead of internal meshes, but the main problem in applying the BEM in the case of nonhomogeneous materials is finding the fundamental solution. Generally speaking, a single fundamental solution is not available in transient nonlinear problems for arbitrary material gradients. Meshless methods have shown many advantages for handling such problems.[15,16] Several MM versions have also been proposed with different formulations.

Here, t-RPIM[15,16] was used to solve the transient heat transfer problem in the layered composite sample. The solution of the problem via temperature predictions is aimed at yielding thermophysical or geometric layer parameters that will add insight into the manufacture of samples, their thermal properties, and spatial distributions. This problem is studied in this work through an inverse analysis for finding the spatial distribution of constituent materials in the layered sample. In the t-RPIM, the temperature field is approximated without the need for a predefined mesh, and the domain integrals are evaluated by the Cartesian transformation method (CTM)[49] to avoid the need for foreknowledge of the background cell structure. The domain integrals in the conventional MMs are calculated using the Gaussian quadrature (GQ) method with a background mesh, which is a time-consuming task.[15] In contrast, in the t-RPIM, the integrals are computed using the CTM, which is a fast and accurate meshless integration technique. Moreover, the applied t-RPIM has the ability to model all possible thermal boundary conditions, including convection, radiation, insulation, etc. Little attention has been paid to the heat conduction process with radiation boundary conditions in FGMs while the role of thermal radiation is important in high-temperature applications,[50] especially those with temperatures higher than 600 °C. For modeling a problem with radiative boundary conditions, it suffices to define an effective convection heat transfer coefficient on boundaries with radiation as done in Eq. (5). Shape functions are important components in meshless methods and are also used in the t-RPIM method. This is an advantage of the t-RPIM since its shape

functions possess the Kronecker delta function property, which eliminates the need for special techniques to provide compliance with the boundary conditions.[15] Details of the numerical implementation of the t-RPIM are discussed in Appendix A.

V. TEMPERATURE MEASUREMENT AND THERMAL PROPERTY DETERMINATION RESULTS AND DISCUSSION

Laser intensity was measured to be 1.131×10^4 W/m^2. The exact amount of absorbed laser power on the front surface could not be measured directly as it depends on both absorption and radiation coefficients. For the calculation of the amount of absorbed laser power on the sample surface, one needs to find the sample surface absorptivity defined as the ratio of the absorbed to the incident radiant power at the surface. The problem of approximating absorptivity was approached by considering several values for the absorptivity between 0 and 1 and comparing the calculated temperature by t-RPIM with the measured one. In these calculations, the known volume fractions known from the sample fabrication and the literature values of thermal properties were used. Best agreement between the measured and the calculated temperature depth profiles was found for absorptivity equal to 0.20. Therefore, in all calculations, the absorptivity was set equal to 0.20.

The measured temperature distribution of the layered sample using thermography images obtained with the MIR camera was introduced into MATLAB and the MATLAB program calculated the contour of Fig. 7(a). No manipulation was done on the boundary value temperatures. In Fig. 7(b), the same transient heat conduction problem was modeled using the t-RPIM with 527 nodes and 2912 integration points in the spatial domain and 12 time steps between 0 and 118 s. The obtained temperatures at the integration points in the t-RPIM were entered into Tecplot 360 software, which can plot a depth profile using the field values at scattered points. The temperature data were used to generate the temperature depth profile. As this is the output of this software, no further manipulation was done on the boundary temperature values. Therefore, the association of colors with temperatures is unique so they can reliably correspond to the actual measured temperature range. This direct solution was implemented using the real volume fraction values and the temperature dependent thermophysical property values of the constituent powders according to Eqs. (3a)–(4b). Also, the thicknesses of the layers are known according to the sample design. The agreement between the measured and calculated temperature depth profiles (Fig. 7) confirms the ability of the applied t-RPIM to solve the direct transient nonlinear heat conduction problem in media with temperature dependent thermal properties.

The transient thermographic data show the temperature distribution along the depth in the sample [Fig. 7(a)]. Also, the temperature profile obtained from the t-RPIM is illustrated in Fig. 7(b). The convection boundary condition both at the upper and at the lower boundaries of the sample resulted in symmetric temperature distributions along the y axis, which is physically acceptable since there is an axial symmetry in the sample.

A major purpose for developing the t-RPIM theoretical method to solve time-domain heat conduction problems is the measurement of thermophysical properties of nonhomogeneous solids and, if applicable, their depth dependence. This can be accomplished by determining the thermophysical properties of constituent materials and Al_2O_3 volume fractions in the various layers of the sample through an inverse problem analysis. According to the governing differential equation [Eq. (6)] for the transient heat transfer problem in the time domain, it is apparent that temperature is not a linear function of the unknown parameters since the thermal properties of the sample change along the depth. Therefore, this makes the inverse analysis nonlinear, and difficulty in identification occurs due to this nonlinear nature. In

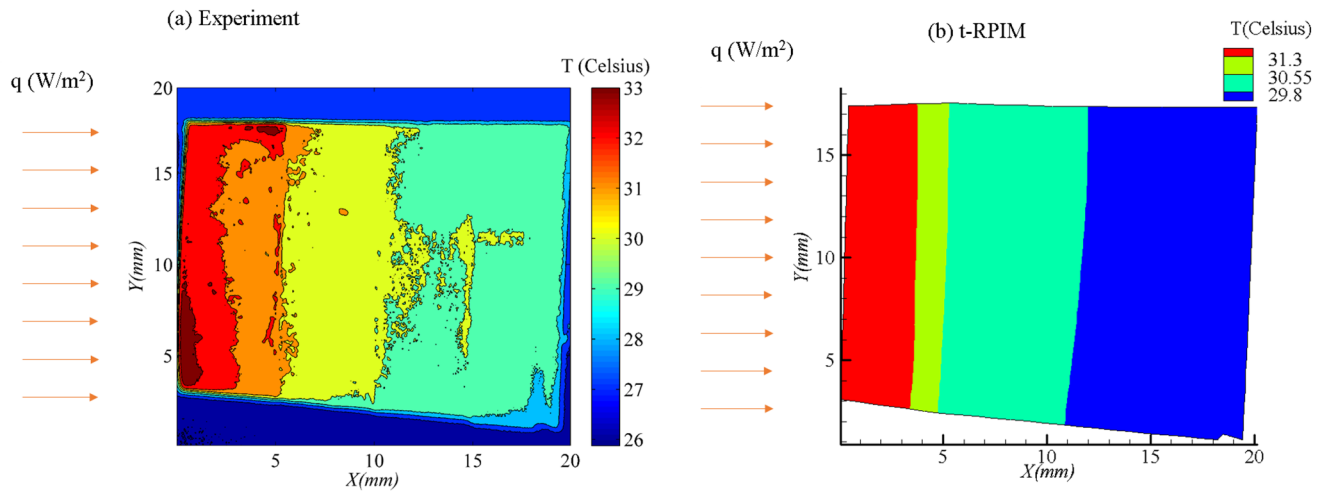

FIG. 7. Comparison of (a) the measured and (b) the calculated temperature for the layered sample using thermal properties from the literature (t = 118 s).

TABLE I. Sampling point coordinates.

Sampling points	x (mm)	y (mm)
P_1	19.08	11.30
P_2	2.72	11.27
P_3	7.65	11.02
P_4	12.44	10.75
P_5	14.79	10.63

nonlinear inverse thermal problems, the path of convergence is not known in advance. The identification procedure could be affected due to the small values of the sensitivity coefficients, the correlation between the sensitivity of temperature with respect to different unknown parameters, uniqueness issues, measurement error, etc. Discussion on each of these issues can be found in the literature on inverse analysis.[20,51,52] However, the main goal of this study was to show experimentally the ability of t-RPIM to deal with transient heat transfer in nonhomogeneous materials and to extract the thermal parameters through an inverse analysis using actual experimental data. With the values of thermal conductivity and specific heat of the constituent materials taken as independent of temperature, the associated inverse problem was solved using the damped Gauss-Newton method[53,54] (Appendix B). In the first stage of the inverse analysis, the following material properties constituted the unknown parameters: $\boldsymbol{X_p} = [k_{Al_2O_3}, c_{Al_2O_3}, k_{Y\text{-}ZrO_2}, c_{Y\text{-}ZrO_2}]^T$. It should be mentioned that the volume fractions of the constituent powders in each layer were known from the sample fabrication stage and used in this inverse analysis. Also, the values of the thermal properties found in the literature were used as the initial guess value of the unknown thermal properties in this stage. After identification of the unknown thermal parameters in the first stage, the volume fractions in the four layers are identified in the second stage of the inverse analysis. In this stage, the identified thermal properties from the first stage are used as known parameters. Additionally, the initial guess values for the volume fractions are arbitrary. The identified volume fractions in this stage were used to check the validity of the inverse problem in the reconstruction of the volume fraction values. This inverse problem was solved using five sampling points given in Table I.

In order to investigate the effect of the initial guess values on the identified thermal properties in the first stage of the inverse analysis, two different sets of initial values of thermal properties were considered. The temperature distribution along the depth of the sample was calculated using t-RPIM and was compared with the measured temperature. A correction to the value of the guessed parameters was thus made. This scheme was continued in subsequent iterations until convergence in the values of the unknown parameters was obtained. In the first case, the thermal property mean values in the temperature range of the experiment obtained from the literature [Eqs. (3a)–(4b)] were used as the initial guess for the property calculation. The thermal properties determined from this inverse analysis are given in Table II. In this case, there is a high convergence rate, and, after 3 iterations, the inverse problem converged. In the second case, the initial guess values for the thermal properties were chosen to be half of the reported values in the literature and convergence occurred after 7 iterations. The percentage of the differences between the identified thermal properties in these two cases is also shown in Table II. It can be concluded that, while the initial guess in the inverse analysis changed by 50%, the maximum change in the identified thermal properties was only about 5%. Therefore, even when the initial guesses are far from the actual values of the unknown parameters, the proposed algorithm is capable of obtaining acceptable estimates of the unknowns.

In the second stage of the inverse analysis, the thermal properties determined from the first inverse problem (case I) were used as known parameters in the numerical calculation of the temperature profile, while the volume fraction values in each layer were assumed to be unknown, i.e., $\boldsymbol{X_v} = [X_{v_1}, X_{v_2}, X_{v_3}, X_{v_4}]^T$, where X_{v_i} (with $i = 1,\ldots,4$) is the volume fraction of Al_2O_3 powder in each sample layer. In this manner, the ability of the proposed inverse algorithm to determine the distribution of the constituents of the layered samples was assessed. The actual densities of pure sintered Al_2O_3 and Y-ZrO_2 samples were measured directly prior to the calculations. This second inverse problem was solved using the same sampling points (Table I), and the calculated volume fraction values are also shown in Table II. Subsequently, after the determination of Al_2O_3 powder volume fractions in each layer, the effective thermophysical properties at each depth were estimated using the ROM [Eq. (1)]. This nondestructive procedure yielded geometric layer parameters that add significant and unique insight into the topography of the manufactured material layers, their thermal properties, spatial, and density distributions.

TABLE II. The determined thermal property and volume fractions in the layered sample.

	$k_{Al_2O_3}$ (W/m K)	$c_{Al_2O_3}$ (J/kg K)	$k_{Y\text{-}ZrO_2}$ (W/m K)	$c_{Y\text{-}ZrO_2}$ (J/kg K)
Thermal properties from literature[38,40–42]	32.67–36.96	766.4–785.2	3.07	470.2
Initial guess of case I	32.67	766.4	3.07	470
Determined thermal properties in case I	26.39 ± 0.31	766.4 ± 33	3.32 ± 0.05	589.87 ± 28
Initial guess of case II	16.8	383.2	1.5	235
Determined thermal properties in case II	26.01 ± 0.42	743.20 ± 48	3.14 ± 0.06	569.85 ± 29
Percent of difference between the results of two cases	1.5%	3%	5.4%	3.4%
Al_2O_3 volume fractions as fabricated	0%	25%	50%	75%
Determined volume fractions	0.01% ± 0.006%	29.4% ± 0.7%	45.32% ± 1.2%	73.74% ± 0.7%

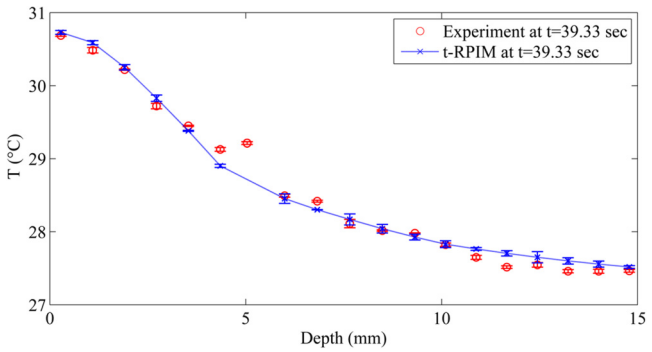

FIG. 8. Comparison of the measured and reconstructed temperature depth profiles using the identified properties.

Due to the fact that nonlinear inverse thermal problems are ill-conditioned, measurement errors can have a significant effect on the outcome of the inverse analysis. In general, experimental measurements should be accurate enough to have a maximum of 2% error.[20,51,52] By applying suitable techniques in the inverse analysis, the ill-conditioned problems could be solved.[18,24,55–61] In this study, the Moore-Penrose pseudoinverse technique is used for the calculation of inverse matrices with very small determinant.

Finally, to validate the results of the inverse problem, the reconstructed temperature depth profile using the determined thermal properties from the first stage of the inverse analysis (case I) and the determined volume fractions from the second stage is compared with the measured temperature depth profile in Fig. 8 at the time instant of $t = 39.33$ s. The very good agreements between the experimental thermographic and theoretical/computational results in Table II and Fig. 8 demonstrate the effectiveness of the t-RPIM method as a powerful tool to analyze transient temperature responses in nonhomogeneous materials. As shown in Fig. 8, temperature measurements have a variance between the maximum and the minimum values. These values were used in the inverse algorithm, and the corresponding unknown parameters were identified using each set of measured temperatures. Figure 8 shows the calculated temperatures corresponding to the identified parameters, along with their variances calculated with values shown in Table II.

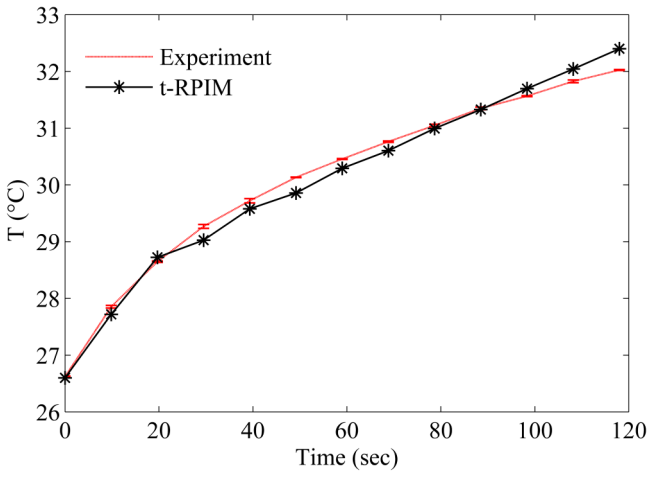

FIG. 9. Temperature evolution for the layered sample at $x = 2.7$ mm and $y = 11.3$ mm.

Additionally, the transient temperature profile, calculated using the determined thermal properties at location $x = 2.7$ mm and $y = 11.3$ mm of the layered sample, is plotted in Fig. 9. The maximum and average differences between measured and calculated temperature for this coordinate point for all instants in its temperature history (Fig. 9) is 0.95% and 0.53%, respectively, which confirms that the applied t-RPIM can also follow the evolution of temperature with time using the transient heat conduction theory in layered solids with good accuracy.

VI. CONCLUSIONS

The expressed goal of this work was the extraction of thermophysical properties and density volume fractions as a function of depth in nonhomogeneous solids fabricated using the PM method. Thermography-based temperature imaging and measurement of a graded material were performed and a theoretical model resulting in the numerical solution of the associated heat conduction problem with convection boundary conditions was developed. The combination of the t-RPIM technique and the developed numerical method was applied to the reconstruction of the thermophysical and geometric layer parameters from the temperature data that can then be used in the manufacturing of nonhomogeneous materials and/or SHM applications.

In the first step, the direct analysis of the problem with known thermophysical properties and spatial distribution was performed to calculate the transient temperature distribution. Comparison of the experimental and theoretical/numerical temperature profiles confirmed the success of the presented methodology in dealing with nonlinear transient heat conduction problems.

In view of the fact that the exact values of the thermal properties in the layered sample made with the PM method were unknown, the determination of the depth dependence of these properties was made by means of a two-stage inverse analysis using the damped Gauss-Newton method. The temperature depth profile in the layered sample, calculated from the determined thermal properties and density volume fractions, was compared with the measured temperature depth profile using thermography and good agreement was found down to 15 mm from the surface.

Many factors can affect the properties of the material manufactured using the PM method, including powder dispersion in the layers, cracks or voids in the final sample, inclusions, nonuniform density due to variable pressure distribution, time, and temperature during the sintering process, etc. Therefore, this process can result in uncertainty in the manufacturing process of quality control and variation from sample to sample. Besides the intrinsic mathematical interest in the development of the thermal inverse problem methodology, its combination with nondestructive MIR thermography was shown to be a powerful analytical method for estimating multiple material parameters central to the assessment of the quality of graded materials.

ACKNOWLEDGMENTS

A. Mandelis acknowledges the support of the Natural Sciences and Engineering Research Council of Canada (NSERC) for a Discovery grant and the Canada Research Chairs Program. The Toronto Nanofabrication Center (TNFC) is gratefully acknowledged for the sputtering of the samples. The authors wish to thank Professor Tom Coyle for technical assistance with the sample fabrication and characterization. S. Kooshki gratefully acknowledges a scholarship by Yazd University, Iran.

APPENDIX A: TRULY MESHLESS RADIAL POINT INTERPOLATION METHOD (t-RPIM)

1. The RPIM shape functions

Approximate solutions of the differential equation for nonlinear heat conduction in solids can be found if the field variable (temperature) is approximated using shape functions in a local support domain. This is possible because in the interpolation process, the information from local nodes around a desired point is sufficient for the construction of the approximate function at that point, and the information from far away nodes is not required. The shape of the support domain is arbitrary and most often is circular in 2D problems. The value of the field variable at a point is calculated according to the following equation:

$$u(\vec{X}) = \sum_{i=1}^{n} u_i \varphi_i(x_j, y_j) = \{\vec{\varphi}\}^T \{\vec{u_s}\}, \tag{A1}$$

where $\varphi_i(x_j, y_j)$ is the shape function of the ith node at point $\vec{X} = (x_j, y_j)$. n is the number of nodes in the supporting domain and u_i is the value of the field variable at the nodal points. The value of the shape function for nodes outside the supporting domain is zero.

The accuracy of the interpolation at each point, among other factors, depends on the shape and size of the support domain.[16] In this work, the method of Liu and Gu[62] was used to determine the dimensions of the support domain. The domain size was determined by $d_s = \alpha_s d_c$, where α_s is a constant, usually between (1.5 and 3), and d_c is the average nodal spacing in the domain. A simple relation for obtaining the average nodal spacing is given by Liu and Gu.[62] The transient temperature in the nonhomogeneous domain is a function of both time and space, $T(\vec{X}, t)$. Therefore, the unknown temperature field in the space and time domain is approximated using RPIM, both polynomial and radial basis functions (RBFs),[63,64] as follows:

$$T(\vec{X}, t) = \sum_{i=1}^{n} R_i(\vec{X}) a_i(t) + \sum_{k=1}^{m} P_k(\vec{X}) b_k(t), \tag{A2a}$$

where n is the number of nodes in the domain of point $(\vec{X})$ and m is the number of monomial basis functions. Linear basis functions with $m = 3$ were used for the sake of simplicity, i.e.,

$$P^T(\vec{X}) = [1, x_j, y_j]. \tag{A2b}$$

The conventional RBFs used in the RPIM are listed elsewhere.[15,16,63–65] In the present study, the thin plate spline (TPS) function was employed for the construction of the shape functions so that $R_i = r_i^{\eta}$, where r_i is the Euclidian distance between point $\vec{X} = (x_j, y_j)$ and the ith node of the domain. A value of 3.001 was used for η according to Liu and Gu.[62] Finally, the TPS function was written as

$$R_i = \left(\sqrt{(x_j - x_i)^2 + (y_j - y_i)^2}\right)^{\eta}. \tag{A2c}$$

The $n + m$ unknown coefficients $[a_i(t), b_k(t)]$ in Eq. (A2a) can be calculated by imposing the Kronecker delta function property and some other constraint equations. The Kronecker function property is satisfied as

$$u(\vec{X}_i) = u_i, \tag{A3}$$

where $\vec{X}_i = (x_i, y_i)$ is the coordinate of node i in the domain and u_i is the temperature at node i. This leads to a system of n equations which in matrix form can be written as

$$\boldsymbol{u_i} = \boldsymbol{R_0 a} + \boldsymbol{P_m b}, \tag{A4a}$$

where $\boldsymbol{u_i^T} = \{u_1, u_2, \ldots, u_n\}$, in which $(\quad)^T$ denotes the transpose of a vector or a matrix, and $\boldsymbol{R_0}$ is the moment matrix of the RBFs,

$$\boldsymbol{R_0} = \begin{bmatrix} R_1(r_1) & R_2(r_1) & \cdots & R_n(r_1) \\ R_1(r_2) & R_2(r_2) & \cdots & R_n(r_2) \\ \vdots & \vdots & \ddots & \vdots \\ R_1(r_n) & R_2(r_n) & \cdots & R_n(r_n) \end{bmatrix}. \tag{A4b}$$

Furthermore, constraint conditions should be satisfied by coefficients a_i in Eq. (A2a). These constraints will give the extra m equations required for determining the $n + m$ unknown coefficients. These constraint equations are necessary to ensure that the coefficients are obtained uniquely,[15,16]

$$\sum_{i=1}^{n} P_j(\vec{X}_i) a_i(t) = P_m^T a = 0 \quad \text{for } j = 1, 2, \ldots, m. \tag{A5a}$$

Also, the polynomial moment matrix is written as

$$\boldsymbol{P_m^T} = \begin{bmatrix} 1 & 1 & \cdots & 1 \\ x_1 & x_2 & \cdots & x_n \\ y_1 & y_2 & \cdots & y_n \\ \vdots & \vdots & \ddots & \vdots \\ p_m(x_1) & p_m(x_2) & \cdots & p_m(x_n) \end{bmatrix}. \tag{A5b}$$

Combining Eqs. (A4a) and (A5a) gives a system of $n + m$ equations in the unknowns which can be expressed in a matrix

form as follows:

$$\begin{bmatrix} \boldsymbol{u_i} \\ 0 \end{bmatrix} = \boldsymbol{G} \begin{bmatrix} \boldsymbol{a} \\ \boldsymbol{b} \end{bmatrix}, \tag{A6a}$$

where $\boldsymbol{G}$ is the moment matrix,

$$\boldsymbol{G} = \begin{bmatrix} \boldsymbol{R_0} & \boldsymbol{P_m} \\ \boldsymbol{P_m^T} & \boldsymbol{0} \end{bmatrix}. \tag{A6b}$$

Finally, after some arithmetic manipulations, the approximate filed temperature function can be expressed in the following form:

$$T(\vec{\boldsymbol{X}}, t) = \sum_{i=1}^{n} \varphi_i(x_j, y_j) T_i(t) = \boldsymbol{\varphi^T}(\boldsymbol{x}) \boldsymbol{T}(t), \tag{A7a}$$

where $\boldsymbol{T}$ is a vector containing nodal temperature values and $\boldsymbol{\varphi^T}$ is the shape function vector containing the first n components of the following vector:

$$\tilde{\boldsymbol{\varphi}} = [\boldsymbol{R^T P^T}] \boldsymbol{G^{-1}}. \tag{A7b}$$

The formalism for the shape functions calculation in the t-RPIM can now be used in the solution of the inverse heat conduction problem.

2. Mathematical formulation of the nonlinear problem

The Galerkin weak formulation of the nonlinear heat conduction equation [Eq. (5)] is written by considering the RPIM shape functions as weighting functions[66]

$$\int_{\Omega} \varphi_i [\nabla \cdot (k(\boldsymbol{x}, T) \nabla T) - \rho(\boldsymbol{x}, T) c(\boldsymbol{x}, T) \dot{T}] d\Omega - \int_{\Gamma_2} \varphi_i [h(T - T_\infty)] d\Gamma_2 = 0, \tag{A8a}$$

where φ_i is the RPIM shape function corresponding to node i [Eq. (A7b)]. Performing integration by parts on the first term of Eq. (A8a), the following relation is obtained:

$$- \int_{\Omega} \{\nabla \varphi_i \cdot [(k(\boldsymbol{x}, T) \nabla T)] + \varphi_i \rho(\boldsymbol{x}, T) c(\boldsymbol{x}, T) \dot{T}\} d\Omega + \int_{\Gamma_1} \{\varphi_i [(k(\boldsymbol{x}, T) \nabla T)] \cdot \boldsymbol{n}\} d\Gamma_1 - \int_{\Gamma_2} \varphi_i [h(T - T_\infty)] d\Gamma_2 = 0 . \tag{A8b}$$

Given that $[(k(\boldsymbol{x}, T) \nabla T)] \cdot \boldsymbol{n} = \bar{q}$, substituting Eq. (A7a) into Eq. (A8b) yields

$$- \int_{\Omega} k(\boldsymbol{x}, T) \left[\frac{\partial \varphi_i}{\partial x} \frac{\partial \varphi_j}{\partial x} + \frac{\partial \varphi_i}{\partial y} \frac{\partial \varphi_j}{\partial y} \right] T_i(t) d\Omega - \int_{\Omega} \rho(\boldsymbol{x}, T) c(\boldsymbol{x}, T) \varphi_i \varphi_j \frac{\partial T_i}{\partial t} d\Omega - \int_{\Gamma_1} q(x, t) \varphi_i d\Gamma_1 - \int_{\Gamma_2} [h \varphi_i \varphi_j T_i(t) - h T_\infty \varphi_i] d\Gamma_2 = 0. \tag{A8c}$$

The following system of equations is then obtained from Eq. (A8c):

$$[M]\{\dot{T}\} + [K(T)]\{T\} = \{F(t, T)\}, \tag{A8d}$$

where

$$M_{ij} = \int_{\Omega} \rho(\boldsymbol{x}, T) c(\boldsymbol{x}, T) \varphi_i \varphi_j d\Omega, \tag{A8e}$$

$$K_{ij} = \int_{\Omega} k(\boldsymbol{x}, T) \left[\frac{\partial \varphi_i}{\partial x} \frac{\partial \varphi_j}{\partial x} + \frac{\partial \varphi_i}{\partial y} \frac{\partial \varphi_j}{\partial y} \right] d\Omega + \int_{\Gamma_2} h \varphi_i \varphi_j d\Gamma_2, \tag{A8f}$$

$$F_i = - \int_{\Gamma_1} \bar{q} \varphi_i d\Gamma_1 + \int_{\Gamma_2} h T_\infty \varphi_i d\Gamma_2. \tag{A8g}$$

In Eq. (A8d), $\{T\}$ is the nodal temperature vector, $[M]$ is the so-called thermal mass matrix, $[K(T)]$ is the thermal stiffness matrix, and $\{F(t, T)\}$ is the forcing matrix. Since each node in a heat transfer problem has one degree of freedom, the dimensions of $\{T\}$ and $\{F(t, T)\}$ are $n \times 1$ and the dimensions of $[M]$and $[K(T)]$ matrices are $n \times n$.

The matrix equation (A8d) represents a set of ordinary differential equations involving unknown nodal temperatures and their derivative with respect to time. In order to discretize the temperature in the time-domain, the Crank-Nicolson scheme[67] was utilized in the following form:

$$\frac{1}{2}\{\dot{T}\}_s + \frac{1}{2}\{\dot{T}\}_{s+1} = \frac{\{T\}_{s+1} - \{T\}_s}{2} + O(\Delta t)^2. \tag{A9}$$

This equation holds for the times between the steps s and $s+1$. Applying Eq. (A9) to Eq. (A8d), the following set of algebraic equations is obtained:

$$\{T\}_{s+1} = [\hat{K}_{s+1}]^{-1} (\bar{K}_s T_s + \hat{F}_{s,s+1}), \tag{A10a}$$

$$\hat{K}_{s+1} = M_{s+1} + \frac{1}{2} \Delta t_{s+1} K_{s+1}, \tag{A10b}$$

$$\bar{K}_s = M_{s+1} - \frac{1}{2} \Delta t_{s+1} K_s, \tag{A10c}$$

$$\hat{F}_{s,s+1} = \frac{1}{2} \Delta t_{s+1} [F_s + F_{s+1}]. \tag{A10d}$$

Since the material properties are functions of temperature, the problem is solved using an iterative method at each time step. Initially, the mass, stiffness, and forcing matrices are calculated using the temperature distribution in the previous time step and are then updated accordingly. The process is repeated until the solution converges within a predefined tolerance value.

At each time step of the transient problem analysis, domain integrals in Eqs. (A8e) and (A8f) must be evaluated.[15] Applying

an efficient method for the evaluation of these integrals plays a significant role in the overall efficiency of the mesh-free method. The CTM has the capability of evaluating domain integrals with higher accuracy and efficiency in comparison with the conventional integration methods such as the Gaussian quadrature method,[15] which is traditionally used in mesh-free approaches. This technique is especially designed for the fast and accurate evaluation of the domain integrals with different integrands over a single domain.[16] A description of the CTM method can be found elsewhere.[15,16,49] Here, we consider a regular integral in a 2D domain

$$I = \int_{\Omega} h(x, y)\, d\Omega, \tag{A11}$$

in which $h(x, y)$ is an arbitrary function and Ω represents the integration domain as depicted in Fig. 6. According to the CTM, the integral of Eq. (A11) can be worked out as follows:

$$I = \sum_{i=1}^{N} W^{2D}(\boldsymbol{x_i}) h(\boldsymbol{x_i}) = \boldsymbol{W^{2D}} \cdot \boldsymbol{H}, \tag{A12}$$

in which N is the number of integration points of the CTM and $W^{2D}(x_i)$ is the integration weight corresponding to the ith integration point at $\boldsymbol{x_i}$. It is the fact that all the integral transformations are carried out in the Cartesian coordinate system that has given the method the name CTM.[49]

3. Numerical implementation of the Cartesian transformation method

According to Eqs. (A8e) and (A8f), the mass and stiffness matrices can be determined by evaluating domain integrals. The CTM equation (A12) can be applied for the calculation of these integrals. The boundary integrals in the forcing vector and the stiffness matrix were calculated using the GQ method, so that the domain integrals of Eqs. (A8e) and (A8g) reduce to the CTM forms,

$$M_{ij} = \sum_{p=1}^{N} W_p^{2D}(R_p \times C_p \times S_{pi} \times S_{pj}), \tag{A13a}$$

$$K_{ij} = \sum_{p=1}^{N} W_p^{2D}[A_p(S_{pi}^{x} \times S_{pj}^{x} + S_{pi}^{y} \times S_{pj}^{y})] + \sum_{p=1}^{G_2} W_p^{GQ}(h \times S_{pi} \times S_{pj}), \tag{A13b}$$

$$F_i = -\sum_{p=1}^{G_1} W_p^{GQ}(\bar{q} \times S_{pi}) + \sum_{p=1}^{G_2} W_p^{GQ}(h \times T_{\infty} \times S_{pi}), \tag{A13c}$$

where N is the number of CTM integration points in the domain, G_1 is the number of Gaussian integration points on the boundary segment Γ_1, and G_2 is the number of Gaussian integration points on the boundary segment Γ_2. W_p^{2D} in each integral is the CTM integration weight and W_p^{GQ} is the Gaussian integration weight. Other vectors and matrices in Eqs. (A13a)–(A13c) are defined as follows:

$$\{R\} = \begin{Bmatrix} \rho(x_1, T) \\ \rho(x_2, T) \\ \vdots \\ \rho(x_N, T) \end{Bmatrix}, \quad \{A\} = \begin{Bmatrix} k(x_1, T) \\ k(x_2, T) \\ \vdots \\ k(x_N, T) \end{Bmatrix}, \quad \{C\} = \begin{Bmatrix} c(x_1, T) \\ c(x_2, T) \\ \vdots \\ c(x_N, T) \end{Bmatrix}, \tag{A13d}$$

$$\boldsymbol{S} = \begin{bmatrix} \varphi_1(x_1) & \varphi_1(x_2) & \cdots & \varphi_1(x_N) \\ \varphi_2(x_1) & \varphi_2(x_2) & \cdots & \varphi_2(x_N) \\ \vdots & \vdots & \ddots & \vdots \\ \varphi_n(x_1) & \varphi_n(x_2) & \cdots & \varphi_n(x_N) \end{bmatrix}, \tag{A13e}$$

$$\boldsymbol{S^x} = \begin{bmatrix} \frac{\partial \varphi_1(x_1)}{\partial x} & \frac{\partial \varphi_1(x_2)}{\partial x} & \cdots & \frac{\partial \varphi_1(x_N)}{\partial x} \\ \frac{\partial \varphi_2(x_1)}{\partial x} & \frac{\partial \varphi_2(x_2)}{\partial x} & \cdots & \frac{\partial \varphi_2(x_N)}{\partial x} \\ \vdots & \vdots & \ddots & \vdots \\ \frac{\partial \varphi_n(x_1)}{\partial x} & \frac{\partial \varphi_n(x_2)}{\partial x} & \cdots & \frac{\partial \varphi_n(x_N)}{\partial x} \end{bmatrix}, \tag{A13f}$$

$$\boldsymbol{S^y} = \begin{bmatrix} \frac{\partial \varphi_1(x_1)}{\partial y} & \frac{\partial \varphi_1(x_2)}{\partial y} & \cdots & \frac{\partial \varphi_1(x_N)}{\partial y} \\ \frac{\partial \varphi_2(x_1)}{\partial y} & \frac{\partial \varphi_2(x_2)}{\partial y} & \cdots & \frac{\partial \varphi_2(x_N)}{\partial y} \\ \vdots & \vdots & \ddots & \vdots \\ \frac{\partial \varphi_n(x_1)}{\partial y} & \frac{\partial \varphi_n(x_2)}{\partial y} & \cdots & \frac{\partial \varphi_n(x_N)}{\partial y} \end{bmatrix}. \tag{A13g}$$

APPENDIX B: THE INVERSE DAMPED GAUSS-NEWTON ALGORITHM

The discussed inverse problem in this work was approached using the damped Gauss-Newton method[53,54] due to its good convergence rate. The problem of Al_2O_3 volume fraction determination in the layered sample was treated using four layers. According to the design of the layered sample (Fig. 1), the vector of volume fractions for the Al_2O_3 powder in layers 1–4 can be expressed as $\boldsymbol{X_v} = [0,\ 25\%,\ 50\%,\ 75\%]^T$. In each layer, there are two constituent powders: Al_2O_3 and Y-ZrO_2. Therefore, in Eq. (1), it was assumed that v_1 corresponds to the Al_2O_3 volume fraction and v_2 to the Y-ZrO_2 volume fraction at each point: $v_2 = 1 - v_1$, so that the volume fraction of each powder could be found by determining the Al_2O_3 volume fraction at each layer. To determine the four unknown volume fractions in the four layers, the temperature values were given at a few sampling points. These additional data

can be expressed as

$$T_{x_i} = \bar{T}_i x_i \in \Gamma_p, \quad i = 1, 2, \ldots, I, \tag{B1}$$

where $\bar{T}_i$ are measured temperature values obtained by direct measurement using the MIR camera. Γ_p is the y coordinate location where the measurement was made. The vector of unknowns can be expressed as

$$\boldsymbol{X_v} = [X_{v_1}, X_{v_2}, X_{v_3}, X_{v_4}]^T, \tag{B2}$$

where X_{v_j} ($j = 1,2,\ldots,4$) are the unknown volume fractions of Al_2O_3 in layers 1–4. Temperature measurements at the sampling points were made in 12 time steps and the vector of measurement data was expressed as

$$\bar{\boldsymbol{T}} = \left[\bar{T}_{x_1,t_1}, \bar{T}_{x_1,t_2}, \ldots, \bar{T}_{x_1,t_{12}}, \bar{T}_{x_2,t_1}, \ldots, \bar{T}_{x_2,t_{12}}, \bar{T}_{x_3,t_1}, \ldots, \bar{T}_{x_3,t_{12}}, \bar{T}_{x_p,t_1}, \ldots\ldots, \bar{T}_{x_p,t_{12}}\right]^T, \tag{B3}$$

where p is the number of sampling points used in the inverse analysis. In each step of the inverse analysis, based on the estimated volume fractions, temperatures at the sampling points were calculated directly and their values were expressed as

$$\boldsymbol{T} = \left[T_{x_1,t_1}, T_{x_1,t_2}, \ldots, T_{x_1,t_{12}}, T_{x_2,t_1}, \ldots, T_{x_2,t_{12}}, T_{x_3,t_1}, \ldots, T_{x_3,t_{12}}, T_{x_p,t_1}, \ldots, T_{x_p,t_{12}}\right]^T. \tag{B4}$$

For the inverse analysis, an objective function was defined in terms of the summation of squares of the differences between the measured and the computed temperatures at sampling points, and subsequently minimized, leading to the calculation of the vector of unknowns

$$\boldsymbol{f}(\boldsymbol{X_v}) = [\bar{\boldsymbol{T}} - \boldsymbol{T}(\boldsymbol{X_v})]^T [\bar{\boldsymbol{T}} - \boldsymbol{T}(\boldsymbol{X_v})]. \tag{B5}$$

Among several optimization methods that can be used to find the unknown vector $\boldsymbol{X_v}$, the damped Gauss-Newton method[53,54] was selected and the vector of unknowns was found using an iterative equation,

$$\boldsymbol{X_v}^{(k+1)} = \boldsymbol{X_v}^{(k)} + \gamma^{(k)} \boldsymbol{D}^{(k)}, \tag{B6}$$

where $(k+1)$ and (k) indicate the iteration number, $\boldsymbol{D}^{(k)}$ is the search direction, and $\gamma^{(k)}$ is the step length. $\gamma^{(k)} = 1$ was used as the first iteration of each step.[53,54] For this choice, $\gamma^{(k)}$ increases the cost function, i.e., $\boldsymbol{f}(\boldsymbol{X_v})^{(k+1)} > \boldsymbol{f}(\boldsymbol{X_v})^{(k)}$, and the iteration was repeated with $\gamma^{(k)}/2$. The search direction, $\boldsymbol{D}^{(k)}$, can be found using the following equation:

$$\boldsymbol{D}^{(k)} = \left[\boldsymbol{P}^{(k)})^T \boldsymbol{P}^{(k)}\right]^{-1} \left[(\boldsymbol{P}^{(k)})^T (\bar{\boldsymbol{T}} - \boldsymbol{T}(\boldsymbol{X_v})\right], \tag{B7}$$

where $\boldsymbol{P}$ is the global sensitivity matrix. The sensitivity matrix for the ith sampling point was defined as

$$\boldsymbol{P}_i = \begin{bmatrix} P^1_{i,1} & P^2_{i,1} & \cdots & P^j_{i,1} \\ P^1_{i,2} & P^2_{i,2} & \cdots & P^j_{i,2} \\ \vdots & \vdots & \ddots & \vdots \\ P^1_{i,t} & P^2_{i,t} & \cdots & P^j_{i,t} \end{bmatrix}, \tag{B8}$$

where

$$P^j_{i,t} = \frac{\partial T_{x_i,t}}{\partial X_{v_j}} = \frac{T_{x_i,t}|_{X_{v_j}+\varepsilon_d} - T_{x_i,t}|_{X_{v_j}}}{\varepsilon_d}, \quad j = 1, 2, \ldots, 4, \quad t = 1, 2, \ldots, 12, \quad i = 1, 2, \ldots, p. \tag{B9}$$

$T_{x_i,t}|_{X_{v_j}+\varepsilon_d}$ is the value of the temperature at the ith sampling point and at the tth time step, while the jth component of the volume fraction vector (X_{v_j}) is increased to $X_{v_j} + \varepsilon_d$. The value of $\varepsilon_d = 0.05 X_{v_j}$ at each step was used. The global sensitivity matrix is given by

$$\boldsymbol{P} = \begin{bmatrix} P_1 \\ P_2 \\ \vdots \\ P_p \end{bmatrix} \tag{B10}$$

To determine all the components of the global sensitivity matrix, in each step of the solution one needs to evaluate $T_{x_i,t}|_{X_{v_j}+\varepsilon_d}$ for $j = 1, 2, \ldots, 4$, that is, the direct problem corresponding to the experiment must be solved four times. The convergence criterion of the inverse problem is defined as follows:

$$\boldsymbol{X_v}^{(k+1)} - \boldsymbol{X_v}^{(k)} < e, \tag{B11}$$

where e is the desired tolerance to which the unknowns are calculated.

REFERENCES

[1]R. K. Joshi, S. Alwarappan, M. Yoshimura, V. Sahajwalla, and Y. Nishina, Appl. Mater. Today **1**(1), 1–12 (2015).
[2]M. Naebe and K. Shirvanimoghaddam, Appl. Mater. Today **5**, 223–245 (2016).

[3]S. M. Naga, M. Awaad, H. F. El-Maghraby, A. M. Hassan, M. Elhoriny, A. Killinger, and R. Gadow, Mater. Des. **102**, 1–7 (2016).
[4]S. R. Dhineshkumar, M. Duraiselvam, S. Natarajan, S. S. Panwar, T. Jena, and M. A. Khan, Surf. Coat. Technol. **304**, 263–271 (2016).
[5]M. R. Abbas, M. B. Uday, A. M. Noor, N. Ahmad, and S. Rajoo, Mater. Des. **109**, 47–56 (2016).
[6]Y. Fukui, K. Takashima, and C. B. Ponton, J. Mater. Sci. **29**(9), 2281–2288 (1994).
[7]E. Müller, Č. Drašar, J. Schilz, and W. A. Kaysser, Mater. Sci. Eng. A **362**(1–2), 17–39 (2003).
[8]R. Slowak, S. Hoffmann, R. Liedtke, and R. Waser, Integr. Ferroelectr. **24**(1–4), 169–179 (1999).
[9]K. B. Ghosh, J. Mukhopadhyay, and R. N. Basu, J. Power Sources **328**, 15–27 (2016).
[10]Y. Nagasaka, T. Sato, and T. Ushiku, Meas. Sci. Technol. **12**(12), 2081 (2001).
[11]F. Cernuschi, P. Bianchi, M. Leoni, and P. Scardi, J. Therm. Spray Technol. **8**(1), 102–109 (1999).
[12]T. D. Bennett and F. Yu, J. Appl. Phys. **97**(1), 013520 (2005).
[13]L. Fu, K. A. Khor, H. W. Ng, and T. N. Teo, Surf. Coat. Technol. **130**(2–3), 233–239 (2000).
[14]M. Richou, F. Gallay, B. Böswirth, I. Chu, G. Dose, H. Greuner, G. Kermouche, M. Lenci, T. Loewenhoff, and M. Wirtz, Fusion Eng. Des. **146**, 858–861 (2019).
[15]T. Q. Bui, A. Khosravifard, Ch. Zhang, M. R. Hematiyan, and M. V. Golub, Eng. Struct. **47**, 90–104 (2013).
[16]A. Khosravifard, M. R. Hematiyan, and L. Marin, Appl. Math. Modell. **35**(9), 4157–4174 (2011).
[17]S. C. Sun, H. Qi, X. Y. Yu, Y. T. Ren, and L. M. Ruan, Int. J. Thermophys. **39**(11), 121 (2018).
[18]B. Chen, W. Chen, and X. Wei, Int. J. Heat Mass Transfer **84**, 691–699 (2015).
[19]M. Mierzwiczak and J. A. Kołodziej, Int. J. Heat Mass Transfer **54**(4), 790–796 (2011).
[20]M. Dashti Ardakani and M. Khodadad, Inverse Probl. Sci. Eng. **17**(7), 855–870 (2009).
[21]P. Tavakolian, K. Sivagurunathan, and A. Mandelis, J. Appl. Phys. **122**(2), 023103 (2017).
[22]J. D. Silvertown, B. P. Y. Wong, K. S. Sivagurunathan, S. H. Abrams, J. Kirkham, and B. T. Amaechi, J. Invest. Clin. Dent. **8**(4), e12257 (2017).
[23]N. Tabatabaei, A. Mandelis, and B. T. Amaechi, J. Biomed. Opt. **16**(7), 071402 (2011).
[24]X. Wei, W. Chen, B. Chen, and L. Sun, Comput. Math. Appl. **69**(3), 206–222 (2015).
[25]M. A. Nematollahi, M. R. Hematiyan, and M. Farid, Proc. Inst. Mech. Eng. C **225**(7), 1550–1564 (2011).
[26]B. Sawaf, M. N. Ozisik, and Y. Jarny, Int. J. Heat Mass Transfer **38**(16), 3005–3010 (1995).
[27]B. Hatton and P. S. Nicholson, J. Am. Ceram. Soc. **84**(3), 571–576 (2001).
[28]S. Ueda and M. Gasik, J. Therm. Stresses **23**(4), 395–409 (2000).
[29]N. B. Duque, Z. H. Melgarejo, and O. M. Suárez, Mater. Charact. **55**(2), 167 (2005).
[30]Y. Watanabe, N. Yamanaka, and Y. Fukui, Composites A **29**(5–6), 595–601 (1998).
[31]M. El-Wazery and A. El-Desouky, J. Mater. Environ. Sci. **6**(5), 1369–1376 (2015).
[32]M. Belmonte, J. Gonzalez-Julian, P. Miranzo, and M. I. Osendi, Acta Mater. **57**(9), 2607–2612 (2009).
[33]G. Jin, M. Takeuchi, S. Honda, T. Nishikawa, and H. Awaji, Mater. Chem. Phys. **89**(2–3), 238–243 (2005).
[34]M. M. Nemat-Alla, M. H. Ata, M. R. Bayoumi, and W. Khair-Eldeen, Mater. Sci. Appl. **2**(12), 1708 (2011).
[35]J. P. M. Florez, M. B. H. Mantelli, and G. G. V. Nuernberg, Int. J. Heat Mass Transfer **66**, 868–878 (2013).
[36]S. Ghosh, D. Teweldebrhan, J. R. Morales, J. E. Garay, and A. A. Balandin, J. Appl. Phys. **106**(11), 113507 (2009).
[37]M. Trunec, Ceram.-Silik. **52**, 165–171 (2008).
[38]R. E. Taylor, X. Wang, and X. Xu, Surf. Coat. Technol. **120–121**, 89–95 (1999).
[39]S. Raghavan, H. Wang, R. B. Dinwiddie, and W. D. Porter, and M. J. Mayo, Scr. Mater. **39**(8), 1119–1125 (1998).
[40]M. Munro, J. Am. Ceram. Soc. **80**(8), 1919–1928 (1997).
[41]P. Auerkari, *Mechanical and Physical Properties of Engineering Alumina Ceramics* (Technical Research Centre of Finland Espoo, 1996).
[42]K. W. Schlichting, N. P. Padture, and P. G. Klemens, J. Mater. Sci. **36**(12), 3003–3010 (2001).
[43]P. Morrell and R. Taylor, High Temp. High Pressures **17**(1), 79–88 (1985).
[44]D. Hasselman, L. F. Johnson, L. D. Bentsen, R. Syed, H. L. Lee, and M. V. Swain, Am. Ceram. Soc. Bull. **66**(5), 799–806 (1987).
[45]G. E. Youngblood, R. W. Rice, and R. P. Ingel, J. Am. Ceram. Soc. **71**(4), 255–260 (1988).
[46]P. Miranzo and M. I. Osendi, Scr. Mater. **58**(11), 973–976 (2008).
[47]J. N. Reddy and D. K. Gartling, *The Finite Element Method in Heat Transfer and Fluid Dynamics* (CRC Press Taylor & Francis Group, New York, 2010), p. 30.
[48]S. W. Churchill and H. H. S. Chu, Int. J. Heat Mass Transfer **18**(9), 1049–1053 (1975).
[49]A. Khosravifard and M. R. Hematiyan, Eng. Anal. Boundary Elem. **34**(1), 30–40 (2010).
[50]W. A. Ge, C. Y. Zhao, and B. X. Wang, Int. J. Heat Mass Transfer **134**, 101–113 (2019).
[51]M. Khodadadi-Saryazdi, "Characterization of the interior of an inhomogeneous body using surface measurements," Ph.D. thesis (Michigan State University, 1991).
[52]M. Dashti-Ardakani and M. Khodadad, Int. J. Comput. Methods **10**(06), 1350042 (2013).
[53]J. M. Ortega and W. C. Rheinboldt, *Iterative Solution of Nonlinear Equations in Several Variables* (SIAM, New York, 2000), Vol. 30, p. 504.
[54]M. R. Hematiyan, A. Khosravifard, and Y. C. Shiah, Int. J. Heat Mass Transfer **89**, 685–693 (2015).
[55]Y. Gu, W. Chen, C. Zhang, and X. He, Int. J. Heat Mass Transfer **84**, 91–102 (2015).
[56]Y. Gu, W. Chen, and Z.-J. Fu, Inverse Probl. Sci. Eng. **22**(6), 889–909 (2014).
[57]A. Shirzadi, Commun. Numer. Anal. **2013**, cna-00172 (2013).
[58]H. Li, J. Lei, and Q. Liu, Int. J. Heat Mass Transfer **55**(15), 4442–4452 (2012).
[59]P. H. Wen, Y. C. Hon, and Y. G. Xu, Heat Transfer Asian Res. **40**(2), 171–186 (2011).
[60]Z. Li and X.-Z. Mao, Int. J. Numer. Methods Eng. **85**(3), 355–379 (2011).
[61]Y. Hon and T. Wei, Int. Ser. Adv. Boundary Elem. **13**, 135–144 (2002).
[62]G.-R. Liu and Y.-T. Gu, *An Introduction to Meshfree Methods and Their Programming* (Springer Science & Business Media, Dordrecht, 2005), pp. 40, 74–81.
[63]J. G. Wang and G. R. Liu, Int. J. Numer. Methods Eng. **54**(11), 1623–1648 (2002).
[64]A. Djeukou and O. von Estorff, Comput. Mech. **44**(3), 423 (2009).
[65]G. R. Liu, G. Y. Zhang, Y. T. Gu, and Y. Y. Wang, Comput. Mech. **36**(6), 421–430 (2005).
[66]A. Singh, I. V. Singh, and R. Prakash, Int. J. Heat Mass Transfer **50**(5–6), 1212–1219 (2007).
[67]J. N. Reddy, *An Introduction to the Finite Element Method* (McGraw-Hill, New York, 1993), pp. 227–230.